A broad iron line in LMC X-1

James F. Steiner,[1,2]⋆ Rubens C. Reis,[3] Andrew C. Fabian,[1] Ronald A. Remillard,[4]
Jeffrey E. McClintock,[2] Lijun Gou,[2,5] Ryan Cooke,[1] Laura W. Brenneman[2]
and Jeremy S. Sanders[1]

[1]*Institute of Astronomy, Cambridge University, Madingley Road, Cambridge CB3 0HA*
[2]*Harvard–Smithsonian Center for Astrophysics, 60 Garden Street, Cambridge, MA 02138, USA*
[3]*Department of Astronomy, University of Michigan, Ann Arbor, MI 48109, USA*
[4]*MIT Kavli Institute for Astrophysics and Space Research, MIT, 70 Vassar Street, Cambridge, MA 02139, USA*
[5]*National Astronomical Observatories, CAS, 20A Datun Road, Chaoyang District, 100012 Beijing, China*

ABSTRACT

We present results from a deep *Suzaku* observation of the black hole in LMC X-1, supple-
mented by coincident monitoring with the *Rossi X-ray Timing Explorer* (*RXTE*). We identify
broad relativistic reflection features in a soft disc-dominated spectrum. A strong and variable
power-law component of emission is present which we use to demonstrate that enhanced
Comptonization strengthens disc reflection. We constrain the spin parameter of the black hole
by modelling LMC X-1's broad reflection features. For our primary and most comprehensive
spectral model, we obtain a high value for the spin: $a_* = 0.97^{+0.01}_{-0.13}$ (68 per cent confidence).
However, by additionally considering two alternate models as a measure of our systematic
uncertainty, we obtain a broader constraint: $a_* = 0.97^{+0.02}_{-0.25}$. Both of these spin values are en-
tirely consistent with a previous estimate of spin obtained using the continuum-fitting method.
At 99 per cent confidence, the reflection features require $a_* > 0.2$. In addition to modelling
the relativistically broadened reflection, we also model a sharp and prominent reflection com-
ponent that provides strong evidence for substantial reprocessing in the wind of the massive
companion. We infer that this wind sustains the ionization cone surrounding the binary system;
this hypothesis naturally produces appropriate and consistent mass, time and length scales for
the cone structure.

Key words: accretion, accretion discs – black hole physics – stars: individual: LMC X-1 –
X-rays: binaries.

1 INTRODUCTION

LMC X-1 was the first extragalactic black hole (BH) binary to be
discovered; Cygnus X-1 is the only other such persistent X-ray
source with an O-giant companion that is located locally, i.e. within
the Galaxy and Magellanic Clouds. LMC X-1 is quite unusual in
that it consistently maintains a stable luminosity of $L_X/L_{Edd} \approx 16$ per
cent (Gou et al. 2009) despite showing strong fluctuations in the rms
amplitude of its power spectrum.

Recently, the spin[1] of LMC X-1 was measured by modelling
the thermal accretion disc emission (Gou et al. 2009) via the X-
ray continuum-fitting technique (e.g. Zhang, Cui & Chen 1997).
Using a primary sample of 18 *Rossi X-ray Timing Explorer* (*RXTE*)

Proportional Counter Array (PCA) spectra, Gou et al. estimated the
spin to be $a_* = 0.92^{+0.05}_{-0.07}$.

The principal alternative to continuum fitting is the reflection
(or Fe-line) method. Here, the breadth of relativistically broadened
reflection features generated in the accretion disc, most notably
the prominent Fe Kα line complex, is used to determine spin (e.g.
Fabian et al. 1989; Brenneman & Reynolds 2006; Miller 2007).
One advantage of the Fe-line method over X-ray continuum fitting
is that it can be readily applied to measure the spins of stellar-mass
and supermassive BHs alike. In the case of stellar-mass BHs, the
Fe-line method has the further virtue that it is independent of BH
mass and distance; however, its primary drawback is that it relies
upon a much fainter signal. Recent studies (e.g. Miller et al. 2009;
Steiner et al. 2011) have made headway in achieving measurements
via both techniques.

Both methods make one fundamental assumption: that the ac-
cretion disc is truncated at the innermost stable circular orbit
(ISCO). The radius of the ISCO is uniquely defined by the BH's

---

⋆ E-mail: jsteiner@ast.cam.ac.uk
[1] Defined as the dimensionless parameter $a_* \equiv cJ/GM^2$ with $|a_*| \leq 1$, where
M and J are the BH's mass and angular momentum.

mass and spin, growing with increasing mass, and shrinking with increasing spin. The ISCO-truncation assumption is presently at the forefront of theoretical scrutiny, but is generally supported by magnetohydrodynamic simulations (e.g. Reynolds & Fabian 2008; Shafee et al. 2008; Penna et al. 2010; Kulkarni et al. 2011; Noble et al. 2011; Schnittman, Krolik & Noble 2012; Zhu et al. 2012; but see Noble, Krolik & Hawley 2009, and references therein). At the same time, several empirical studies of BH binaries in disc-dominated states provide strong support for the existence of a stable inner-disc radius, including a comprehensive study analysing decades of spectra of LMC X-3 (Steiner et al. 2010) and other studies of BH spectral evolution during outburst (e.g. Done, Gierliński & Kubota 2007; Gilfanov 2010).

Fortuitously, BH X-ray binary sources located in the Large Magellanic Cloud (LMC) are in *Suzaku*'s 'Goldilocks zone' for Fe-line observations. By virtue of being located at ∼50 kpc distance, even luminous BHs are faint enough that pileup effects are modest,[2] while at the same time these sources are bright enough to provide the signal-to-noise ratio required for reflection spin measurements in a reasonable observation time of ∼100 ks. By comparison, pileup in standard *Suzaku* observing modes is severe for outbursting Galactic sources, while Fe-line spin measurements for practical observing times would be photon starved for stellar-mass BHs beyond the Magellanic Clouds.

LMC X-1 is propitious for study because, despite being in an almost persistently disc-dominated state, its spectrum contains a relatively strong power-law component (that is required to produce reflection). Tentative evidence for broad Fe Kα emission (with equivalent width ≈200 eV) was reported by Nowak et al. (2001). We unambiguously confirm the presence of a broad Fe line in LMC X-1, and we use it along with other reflection features to constrain the BH's spin. We thereby demonstrate that Fe fluorescence emission is present in the soft states of LMC X-1 and we furthermore show that the strength of this feature is directly related to the strength of the Compton power-law component.

Our *Suzaku* and *RXTE* observations of LMC X-1 are described in Section 2 and the spectral models we employ are described in Section 3. Our analysis is presented in Section 4 followed by a discussion in Section 5, and we offer our conclusions in Section 6.

2 OBSERVATIONS

We observed LMC X-1 for 130 ks using *Suzaku* from 2009 July 21 through 2009 July 24 with the XIS detectors operating in quarter-window mode. The data were reduced following the XIS and PIN pipeline procedures. For the XIS, we found it necessary to increase the *sisclean* threshold to prevent contamination of the image core.[3] During the observation, the source count rate was stable, varying from its average intensity by less than 5 per cent. Background spectra were obtained from observations of the Lockman Hole. In this and other reduction steps, we have been guided by the procedures described in Kubota et al. (2010).

Suzaku's attitude calibration was improved using the *aeattcor* routine[4] (Nowak et al. 2011). The innermost region of the point spread function (PSF) suffered from moderate (∼10 per cent) photon pileup. To ameliorate this problem, we used the utility

pile_estimate[5] as a guide, and excised the innermost 30 arcsec. Doing so, we retained ≈70 per cent of the flux, while keeping the net pileup below 3 per cent.

Three XIS units were used to collect the data: the two front-illuminated detectors, XIS-0 and XIS-3, and the back-illuminated detector, XIS-1. Spectra were binned to approximately half *Suzaku*'s energy resolution and analysed over 0.8–10 keV (XIS-0,3); 0.8–8 keV (XIS-1). Because of calibration defects, we omitted channels between 1.5 and 2.5 keV and added a Gaussian line near 3.2 keV to model a calibration glitch (Kubota et al. 2010). We also included a narrow Gaussian line near 0.82 keV which was allowed to have separate normalizations between the front- and back-illuminated units. Following Kubota et al., a 1 per cent systematic uncertainty was added to all XIS energy channels. PIN data were analysed from 18 to 50 keV, while using the 'tuned' instrumental background (Fukazawa et al. 2009). The cosmic X-ray background (CXB) contribution to the PIN spectrum[6] is included as a spectral model component[7] with 10 per cent freedom in its normalization. We fitted for the normalization of the instrumental background spectrum, which has a nominal uncertainty of 3 per cent.[8]

During the *Suzaku* observation, we obtained 11 *RXTE* pointings[9] (ranging from 1 to 11 ks apiece), which are interspersed throughout our *Suzaku* observing window and bracket it. We exclusively used the best-calibrated, 'standard 2' spectra from PCU-2. These data improved the constraints on the continuum features, including the high-energy power-law component and the Compton hump. The *RXTE* spectra were background subtracted, corrected for detector dead time, and analysed from 2.55 to 45 keV.

As in previous work (see Steiner et al. 2010, 2011), we standardized the shape and normalization of each detector's calibration so that the power-law parameters of Crab spectra match the Toor & Seward (1974) values; we introduce a floating cross-normalization between detectors to account for any residual difference (≲5 per cent), except for the PIN which is assigned a fixed normalization of 1.16 relative to XIS-0. Motivated by Tsujimoto et al. (2011) and Ishida et al. (2011), which show the back-illuminated XIS detector yields a significantly different spectral index than the two front-illuminated detectors, we include an extra parameter for the difference between the XIS-1 spectral index and those of XIS-0/3. This is incorporated into the model as a fit parameter and found to be quite modest: $\Delta\Gamma \approx 0.015 \pm 0.005$ (Table 1). The additional freedom in the model significantly improves our fits ($\Delta\chi^2 \approx 25$), and insignificantly alters the value of spin (the change is ≲ 10 per cent of the statistical uncertainty).

3 MODELS

We introduce two similar models, which we refer to below as Model 1 and Model 2, that differ in our treatment of the reflection component. Both models assume that this component is generated in the same manner: by disc photons that are Compton scattered in the corona and then reprocessed in the accretion disc. In the first model, we employ the REFLION (Ross & Fabian 2005) family of reflection

---

[2] Miller et al. (2010) discuss pileup and its impact on line fitting.
[3] See http://www-utheal.phys.s.u-tokyo.ac.jp/~yuasa/wiki/index.php/ How_to_check_pile_up_of_Suzaku_XIS_data.
[4] http://space.mit.edu/CXC/software/suzaku/aeatt.html

[5] http://space.mit.edu/CXC/software/suzaku/pest.html
[6] The CXB contributes negligibly to the XIS.
[7] http://heasarc.nasa.gov/docs/suzaku/analysis/pin_cxb.html
[8] http://heasarc.gsfc.nasa.gov/docs/suzaku/analysis/abc/
[9] To avoid contamination from the nearby PSR B0540–69 (Haardt et al. 2001), *RXTE* was offset by 0°.25 in the opposite direction, and we have generated an off-axis response calibration to correct for this, while including a 1 per cent systematic uncertainty in each spectrum.

spectral models, and in the second, use the PEXRAV (Magdziarz & Zdziarski 1995) family. In both cases, we model the thermal disc emission using KERRBB2 (Li et al. 2005; Davis & Hubeny 2006; McClintock et al. 2006) and the Compton component via SIMPL-R (Steiner et al. 2009b, 2011).

For the REFLION-based model, we use REFBHB (Ross & Fabian 2007; Reis et al. 2008). Unlike its counterpart, REFLIONX, which describes reflection from supermassive BHs in active galactic nuclei (AGN), REFBHB accounts for the Compton broadening and other effects unique to the hot, dense discs around stellar-mass BHs. The model REFBHB includes a pre-packaged thermal component. This disc component is a single-temperature blackbody, and hence is intrinsically narrower than the standard multi-temperature disc spectrum. We remove this hardwired blackbody component by the following procedure: we construct a lookup table of blackbody parameters that match the REFBHB inputs, and we use this table to subtract off the best-fitting 2–20 keV blackbody spectrum, while pairing the reflection portion of REFBHB with the disc model KERRBB2. Although this approach does not account for radial variations in the reflection spectrum, it has the virtue of allowing REFBHB to be applied more flexibly to spectra with a strong disc component.

We henceforth refer to this custom version of REFBHB as REFBHB-M. The composite of REFBHB-M operating jointly with SIMPL-R and KERRBB2 comprises what we refer to hereafter as Model 1. We also consider an alternate 'prime' version of Model 1 – Model 1p – with REFBHB-M replaced by its AGN counterpart REFLIONX. Apart from this substitution, Model 1 and Model 1p are identical.

For the reflection components of each of the models considered here, we assume Solar metallicity, which is the only setting available for REFBHB and REFBHB-M. The LMC as a whole is known to have a lower metallicity; however, LMC X-1 is likely to be relatively metal rich because of its young age ($\sim$5 Myr; Orosz et al. 2009).

Our second model family uses IREFLECT which self-consistently computes the reflection edges for ionized gas, given an arbitrary input spectrum. IREFLECT is a generalization based on the model PEXRIV, but whereas PEXRIV is restricted to a pure power law for coronal emission, IREFLECT is freely combined with any coronal spectrum desired. As input to IREFLECT, we use the Compton component generated in the accretion-disc corona, which (as above) is generated by SIMPL-R acting on the disc component KERRBB2. We hereafter refer to this composite model as Model 2. Although IREFLECT offers the advantage of computing reflection self-consistently given an arbitrary input spectrum for the illuminating hard X-rays, it has several major drawbacks compared to REFBHB/REFBHB-M. For example, IREFLECT only computes edge absorption; that is, it neglects all fluorescent line emission, including the Fe line itself. We insert the ionized Fe Kα line emission by adding an intrinsically narrow Gaussian. Like REFBHB-M, IREFLECT does not account for radial variation in the disc's structure.

Table 1. Spectral models.

| Parameters | Model 1(i) | Model 1p(i) | Model 2(i) | Model 1(ii) | Model 1p(ii) | Model 2(ii) |
Instruments	*Suzaku*	*Suzaku*	*Suzaku*	*Suzaku*	*Suzaku*	*Suzaku*
$N_{\rm H}(10^{22}\,{\rm cm}^{-2})$	1.37 ± 0.01	$1.54^{+0.02}_{-0.03}$	$1.38^{+0.02}_{-0.01}$	$1.29^{+0.02}_{-0.01}$	1.55 ± 0.03	$1.41^{+0.01}_{-0.03}$
Γ	$2.62^{+0.10}_{-0.06}$	2.73 ± 0.06	2.65 ± 0.04	$2.50^{+0.10}_{-0.05}$	2.74 ± 0.06	2.62 ± 0.05
$f_{\rm SC}^a$	$0.17^{+0.03}_{-0.01}$	0.204 ± 0.014	0.13 ± 0.01	0.121 ± 0.017	$0.20^{+0.02}_{-0.01}$	0.13 ± 0.01
$a_{*,{\rm CF}}^b$	$0.86^{+0.01}_{-0.02}$	0.81 ± 0.01	0.82 ± 0.01	$0.927^{+0.005}_{-0.011}$	0.81 ± 0.01	0.82 ± 0.01
$\dot{M}^b(10^{18}\,{\rm g\,s}^{-1})$	$1.88^{+0.05}_{-0.03}$	$1.77^{+0.04}_{-0.05}$	1.63 ± 0.02	$1.66^{+0.16}_{-0.06}$	1.78 ± 0.04	1.63 ± 0.02
q_1^c	3	3	3	$6.78^{+0.12}_{-0.06}$	3.7 ± 0.5	$4.5^{+0.4}_{-0.2}$
$R_{\rm br}(R_{\rm ISCO})^c$	$\cdots$	$\cdots$	$\cdots$	2.99 ± 0.04	$4.9^{+0.1}_{-2.}$	$4.9^{+0.1}_{-0.7}$
$a_{*,{\rm ref}}$	$0.94^{+0.02}_{-0.20}$	$0.99^{+0.01}_{-0.31}$	$0.99^{+0.01}_{-0.11}$	0.97 ± 0.01	0.54 ± 0.19	$0.82^{+0.01}_{-0.18}$
$H_{\rm den}\,(10^{19}\,{\rm cm}^{-3})$	15^{+2}_{-9}	$\cdots$	$\cdots$	$5.0^{+2.3}_{-0.7}$	$\cdots$	$\cdots$
$kT_{\rm ref}$ (keV)	$0.73^{+0.01}_{-0.02}$	$\cdots$	$\cdots$	$0.85^{+0.01}_{-0.02}$	$\cdots$	$\cdots$
Illum/BB	0.0204 ± 0.0007	$\cdots$	$\cdots$	$0.0125^{+0.002}_{-0.001}$	$\cdots$	$\cdots$
$N_{\rm ref}(10^{-7})/(10^{-3})^d$	$1.6^{+0.4}_{-0.3}$	$1.1^{+0.3}_{-0.2}$	$\cdots$	$7.8^{+1.1}_{-1.7}$	$1.2^{+0.3}_{-0.2}$	$\cdots$
ξ^e (erg cm s^{-1})	$\cdots$	9700^{+100}_{-2500}	15000^{+1000}_{-8000}	$\cdots$	9000^{+1000}_{-2000}	14000^{+2000}_{-5000}
$T_{\rm ref}$ (10^6 K)	$\cdots$	$\cdots$	6^{+3}_{-4}	$\cdots$	$\cdots$	15^{+1}_{-4}
$E_{\rm Fe}^f$(keV)	$\cdots$	$\cdots$	$6.65^{+0.02}$	$\cdots$	$\cdots$	$6.65^{+0.04}$
$F_{\rm Fe}^f(10^{-4}\,{\rm ph\,s}^{-1}\,{\rm cm}^{-2})$	$\cdots$	$\cdots$	1.1 ± 0.3	$\cdots$	$\cdots$	2.1 ± 0.4
$\xi_D^{e,g}$ (erg cm s^{-1})	3300 ± 900	200 ± 100	15^{+100}_{-5}	2800^{+1600}_{-600}	230 ± 90	20^{+100}_{-5}
$N_{\rm ref,D}^g(10^{-7})$	$0.5^{+0.3}_{-0.1}$	35^{+11}_{-22}	33 ± 20	$0.5^{+0.2}_{-0.1}$	20^{+20}_{-5}	30 ± 10
$N_{\rm XIS3}/N_{\rm XIS0}^h$	$0.960^{+0.001}_{-0.002}$	$0.960^{+0.001}_{-0.002}$	0.960 ± 0.002	0.960 ± 0.002	$0.960^{+0.001}_{-0.003}$	$0.960^{+0.001}_{-0.003}$
$N_{\rm XIS1}/N_{\rm XIS0}^i$	0.916 ± 0.002	$0.921^{+0.002}_{-0.004}$	0.919 ± 0.004	$0.917^{+0.004}_{-0.003}$	0.919 ± 0.003	0.918 ± 0.003
$\Delta\Gamma({\rm XIS1 - XIS0})^i$	-0.017 ± 0.002	$-0.014^{+0.002}_{-0.002}$	-0.015 ± 0.003	$-0.014^{+0.002}_{-0.004}$	-0.014 ± 0.003	$-0.015^{+0.002}_{-0.003}$
$N_{\rm PIN\,CXB}^j(10^{-4}\,{\rm ph\,s}^{-1}\,{\rm cm}^{-2})$	$9.3^{+0.6}_{-0.7}$	8.8 ± 0.6	8.8 ± 0.7	9.1 ± 0.7	8.9 ± 0.7	8.9 ± 0.7
PIN$_{\rm BG,Inst}$ Norm^k	$1.03^{+0.01}_{-0.02}$	$1.03^{+0.02}_{-0.01}$	$1.04^{+0.01}_{-0.02}$	$1.03^{+0.01}_{-0.02}$	1.04 ± 0.01	1.03 ± 0.01
$N_{\rm PIN}/N_{\rm XIS0}^h$	1.16	1.16	1.16	1.16	1.16	1.16
χ^2/ν	$395.4/396$	$396.3/398$	$415.0/395$	$389.0/394$	$375.3/396$	$387.3/393$

Table 1 – *continued*

Parameters Instruments	Model 1(iii) *Suzaku* & *RXTE*	Model 1p(iii) *Suzaku* & *RXTE*	Model 2(iii) *Suzaku* & *RXTE*	Model 1(iv) *Suzaku* & *RXTE*	Model 1p(iv) *Suzaku* & *RXTE*	Model 2(iv) *Suzaku* & *RXTE*
$N_H(10^{22}\,\mathrm{cm}^{-2})$	$1.364^{+0.011}_{-0.005}$	1.55 ± 0.02	1.44 ± 0.01	1.39 ± 0.01	1.58 ± 0.02	1.48 ± 0.02
Γ	2.66 ± 0.03	$2.74^{+0.04}_{-0.05}$	$2.70^{+0.01}_{-0.03}$	2.66 ± 0.03	$2.76^{+0.04}_{-0.02}$	2.76 ± 0.03
f_{SC}^a	0.183 ± 0.007	0.21 ± 0.01	$0.143^{+0.003}_{-0.006}$	$0.180^{+0.009}_{-0.006}$	0.210 ± 0.007	$0.168^{+0.011}_{-0.007}$
$a_{*,CF}^b$	$0.861^{+0.006}_{-0.004}$	$0.811^{+0.008}_{-0.006}$	0.810 ± 0.005	0.857 ± 0.005	0.805 ± 0.006	0.791 ± 0.007
$\dot{M}^b(10^{18}\,\mathrm{g\,s}^{-1})$	1.79 ± 0.02	$1.77^{+0.03}_{-0.03}$	1.65 ± 0.02	1.81 ± 0.03	$1.80^{+0.03}_{-0.02}$	1.69 ± 0.02
q_1^c	3	3	3	$4.4^{+0.2}_{-0.4}$	$4.4^{+0.3}_{-0.4}$	$4.9^{+0.2}_{-0.3}$
$R_{br}(R_{ISCO})^c$	$\cdots$	$\cdots$	$\cdots$	3.0 ± 0.5	4.3 ± 0.5	3.7 ± 0.4
$a_{*,ref}$	$0.97^{+0.01}_{-0.05}$	$0.82^{+0.06}_{-0.27}$	$0.992^{+0.003}_{-0.060}$	$0.84^{+0.03}_{-0.07}$	$0.41^{+0.10}_{-0.14}$	$0.94^{+0.01}_{-0.08}$
H_{den} $(10^{19}\,\mathrm{cm}^{-3})$	$6.4^{+0.4}_{-1.2}$	$\cdots$	$\cdots$	5.3 ± 0.3	$\cdots$	$\cdots$
kT_{ref} (keV)	$0.737^{+0.004}_{-0.007}$	$\cdots$	$\cdots$	0.741 ± 0.007	$\cdots$	$\cdots$
Illum/BB	$0.034^{+0.001}_{-0.002}$	$\cdots$	$\cdots$	0.032 ± 0.002	$\cdots$	$\cdots$
$N_{ref}(10^{-7})/(10^{-3})^d$	3.3 ± 0.3	1.1 ± 0.2	$\cdots$	$3.4^{+0.2}_{-0.3}$	$1.9^{+0.8}_{-0.5}$	$\cdots$
ξ^e (erg cm s^{-1})	$\cdots$	9500^{+200}_{-1500}	7400^{+1100}_{-600}	$\cdots$	5800 ± 1000	4100 ± 1500
T_{ref} (10^6 K)	$\cdots$	$\cdots$	8.9 ± 0.2	$\cdots$	$\cdots$	$14.0^{+0.3}_{-1.1}$
E_{Fe}^f(keV)	$\cdots$	$\cdots$	$6.65^{+0.03}$	$\cdots$	$\cdots$	$6.66^{+0.10}_{-0.01}$
$F_{Fe}^f(10^{-4}\,\mathrm{ph\,s}^{-1}\,\mathrm{cm}^{-2})$	$\cdots$	$\cdots$	$1.0^{+0.1}_{-0.4}$	$\cdots$	$\cdots$	$1.3^{+0.4}_{-0.3}$
$\xi_D^{e,g}$ (erg cm s^{-1})	$5000_{-1500.}$	600 ± 200	900 ± 200	5000_{-1000}	540^{+50}_{-150}	1200^{+200}_{-100}
$N_{ref,D}^g(10^{-7})$	$0.50^{+0.14}_{-0.06}$	8 ± 4	$3.3^{+1.9}_{-0.6}$	0.5 ± 0.1	12 ± 1	4^{+2}_{-1}
N_{XIS3}/N_{XIS0}^h	0.960 ± 0.002	0.960 ± 0.002	0.959 ± 0.002	0.961 ± 0.002	0.960 ± 0.002	0.960 ± 0.002
N_{XIS1}/N_{XIS0}^i	$0.915^{+0.002}_{-0.001}$	0.918 ± 0.004	0.917 ± 0.001	$0.918^{+0.002}_{-0.001}$	$0.916^{+0.005}_{-0.003}$	$0.918^{+0.001}_{-0.002}$
$\Delta\Gamma(\mathrm{XIS1 - XIS0})^i$	-0.018 ± 0.001	-0.015 ± 0.003	-0.014 ± 0.001	-0.015 ± 0.002	-0.017 ± 0.003	-0.016 ± 0.001
$N_{PIN\,CXB}^j(10^{-4}\,\mathrm{ph\,s}^{-1}\,\mathrm{cm}^{-2})$	$9.4^{+0.2}_{-0.4}$	9.1 ± 0.6	$9.5^{+0.3}_{-0.6}$	9.4 ± 0.2	$8.1^{+0.5}_{-0.1}$	$9.8^{+0.2}_{-0.6}$
$\mathrm{PIN}_{BG,Inst}$ Norm^k	1.03 ± 0.01	$1.06_{-0.02}$	$1.041^{+0.004}_{-0.006}$	$1.041^{+0.004}_{-0.009}$	1.05 ± 0.01	$1.039^{+0.006}_{-0.009}$
N_{PIN}/N_{XIS0}^h	1.16	1.16	1.16	1.16	1.16	1.16
N_{RXTE}/N_{XIS0}^h	0.999 ± 0.011	$0.989^{+0.006}_{-0.010}$	$1.049^{+0.005}_{-0.004}$	1.001 ± 0.011	$0.983^{+0.006}_{-0.008}$	1.060 ± 0.005
χ^2/ν	898.6/1121	887.2/1123	984.6/1131	885.5/1119	862.1/1121	944.4/1129

Note. MCMC fit results. Uncertainties are the minimum-width 68 per cent confidence intervals about the posterior mode from the MCMC runs (computed in the log for scale parameters), and χ^2/ν values are listed for the best fit obtained. Numbers with no uncertainty have been set to fixed values. We note that there are additional and unlisted fit parameters for each of the *RXTE* spectral fits [Models 1(iii) through 2(iv)]. In each of those cases, the 11 *RXTE* spectra are each fitted for an independent value of f_{SC}. Additionally, for Models 1(iii), 1p(iii), and 1(iv) and 1p(iv), each *RXTE* spectrum is fitted for its own value of N_{ref}. These values are distributed approximately as $f_{SC} = 0.19 \pm 0.06$ and $N_{ref} = (3 \pm 1.5) \times 10^{-3}$ for Model 1(iii) and (iv); $f_{SC} = 0.17 \pm 0.05$ and $N_{ref} = (2 \pm 2) \times 10^{-7}$ for Model 1p(iii) and (iv); $f_{SC} = 0.15 \pm 0.06$ for Model 2(iii) and (iv).
^{a}The fraction of disc photons scattered into the Compton power law.
^{b}Continuum-fitting parameters: the spin and mass accretion rate. Mass, inclination and distance have been frozen at their nominal values from Gou et al. (2009) [see also Orosz et al. (2009)].
^{c}Relativistic smearing indexes q_1 and q_2 describe, respectively, the inner and outer power-law illumination pattern of the disc. The power law is broken between the two regimes at R_{br}; q_2 is set to 3 in all instances.
^{d}Normalization for REFLIONX, in units of 10^{-7}, and for REFBHB-M, in units of 10^{-3}.
^{e}The ionization parameter of the reflecting material.
^{f}Fe-line parameters E_{Fe} and F_{Fe} give the line energy and line flux, respectively.
^{g}The subscript 'D' refers to reflection emission distant from the BH, and hence not relativistically smeared (see Section 5.3).
^{h}Cross-normalizations for the detectors are referenced to XIS-0.
^{i}The normalization and difference in power-law index of XIS-1 are fitted with respect to XIS-0. The resulting XIS-1 to XIS-0 cross-calibration differs in flux by ≈ 5 per cent over 1–10 keV for a Crab-like source.
^{j}The normalization of the PIN's CXB spectral model.
^{k}The relative normalization of the PIN's instrumental background spectrum.

In summary, we face a tradeoff: Model 1 provides an optimal description of the atomic features, both lines and edges, whereas Model 2 provides a superior description of the 'continuum' shape of the reflection component, especially at low energies. More specifically, although these two models describe the same process, Model 2 consistently describes the continuum shape determined jointly by the thermal, Compton and reflection components, while fluorescent line emission is not incorporated self-consistently. Conversely, in Models 1 and 1p the atomic physics is self-consistent, i.e. the treatment of emission and absorption is unified, but the shape and

intensity of the reflection component are not directly tied to the flux or curvature in the associated power-law component. Lacking an ultimate model of reflection in which the virtues of both models are captured, we employ both approaches separately in arriving at our final result.

For all formulations (Model 1, Model 1p and Model 2), the inner-disc reflection is convolved with the relativistic smearing kernel RELCONVF (Dauser et al. 2010; Fabian et al. 2012). We also include an unblurred reflection component to account for reflection far from the BH, which we demonstrate is produced by fluorescence of the stellar wind by the X-ray source (Section 5.3). We model this sharp reflection component using REFLIONX.

Photoelectric absorption is treated using TBVARABS (Wilms, Allen & McCray 2000).[10] Our three model formulations in XSPEC notation are:

(1) TBVARABS×(SIMPL-R⊗KERRBB2+RELCONVF⊗ REFBHB-M+REFLIONX),
(1p) TBVARABS×(SIMPL-R⊗KERRBB2+RELCONVF⊗ REFLIONX+REFLIONX),
(2) TBVARABS×(SIMPL-R⊗KERRBB2+RELCONVF⊗ [IREFLECT(SIMPL-C)+GAUSS$_{Fe}$]+REFLIONX),

where SIMPL-C is the short form for the power-law emission isolated from SIMPL-R⊗KERRBB2.

3.1 Method

Our results are obtained by first achieving a set of preliminary spectral fits using XSPEC (v12.7; Arnaud 1996). These fits provide the seed for a more intensive and robust analysis using a Markov chain Monte Carlo (MCMC) routine, which is implemented via a package described in Steiner & McClintock (2011). For this application, the MCMC routine has been modified to work with XSPEC. For each fit, a total of 3×10^5 elements are generated,[11] which is sufficient to reach convergence.[12] The results so obtained have been verified using XSPEC in conjunction with a second MCMC sampler: EMCEE (Foreman-Mackey et al. 2012).

All but four free parameters were modelled with non-informative priors, either flat – for shape parameters such as Γ or T – or log-flat (i.e. a flat weighting on the log of the parameter) for scale parameters such as $\dot{M}$ and component normalizations. Two exceptions to this rule are N_H, which was assigned a normal prior distribution[13] of $N(1.15, 0.15) \times 10^{22}$ cm^{-2} (Hanke et al. 2009), and the PIN instrumental background normalization, which was taken to be a normal distribution of $N(1, 0.03)$ bounded within 1 ± 0.06. Lastly, based on the results of Fabian et al. (2012), we impose a restriction on the paired values of a_* and the inner emissivity index q_1. In Fabian et al. (2012), it was shown that for all non-maximal values of spin ($a_* \lesssim 0.94$), q_1 is not expected to deviate substantially from its nominal thin-disc value of $q = 3$. High or extreme values of q_1 are expected only for strong distortions of spacetime near the horizon, for $R \lesssim 2GM/c^2$ (e.g. Wilkins & Fabian 2011). To prevent runaway to unreasonable regions of parameter space, we

assign a weakly constraining prior on q_1, a normal distribution of the following form:

$$p(q_1|a_*) = N(3, 0.475 + 0.05 \times (1 - a_*)^{-1}). \qquad (1)$$

Under this prior, at the minimum possible spin, $a_* = -1$, the prior's standard deviation is 0.5, and it increases slowly with spin, reaching unity at $a_* \approx 0.9$. Thus, for most allowed values of spin, the fit is loosely constrained to conform to its nominal value, $q_1 = 3$. At the highest values of spin, the prior offers essentially no constraint because the standard deviation diverges.

4 ANALYSIS

Before applying these spectral models in detail, we first step back and adopt a more data-centric approach that firmly establishes the existence of a relativistically broadened Fe line. LMC X-1 has a sibling BH binary in the Large Magellanic Cloud, LMC X-3. LMC X-3 is also persistently bright, and it is nearly always in a soft state. However, in contrast to LMC X-1, LMC X-3 is highly variable with L_X/L_{Edd} ranging from $\lesssim 1$ to ~50 per cent (Wilms et al. 2001; Steiner et al. 2010). Moreover, the spectrum of LMC X-3 appears featureless to such an extent that it was recently used by Kubota et al. (2010) as a benchmark for testing the performance of spectral disc models, which makes it an ideal reference source for our purposes. Using the ~70 ks *Suzaku* spectrum of LMC X-3 obtained in 2008 December, studied by Kubota et al., and following precisely the same reduction procedure we used for LMC X-1, we compute the ratio of the spectra of the two sources for the combined front-illuminated XIS units. The virtue of this approach is that this ratio spectrum is completely free of any detector-calibration or data-reduction artefacts.

Because the two continua have different shapes, the ratio spectrum has some smooth curvature, which we remove by fitting it to a low-order polynomial. The residuals clearly reveal the presence of a broad Fe-line component in LMC X-1, as shown in Fig. 1. The line is peaked near 6.7 keV, and it has a broad red wing, as expected for a gravitationally redshifted line fluoresced in the inner disc.

The broad component extends to below 5 keV at an inclination of $i = 36°$ (Orosz et al. 2009), which implies that the disc inner radius is $r < 2.5GM/c^2$ and the spin is correspondingly high. While one cannot obtain a definitive measurement of spin using this ratio spectrum
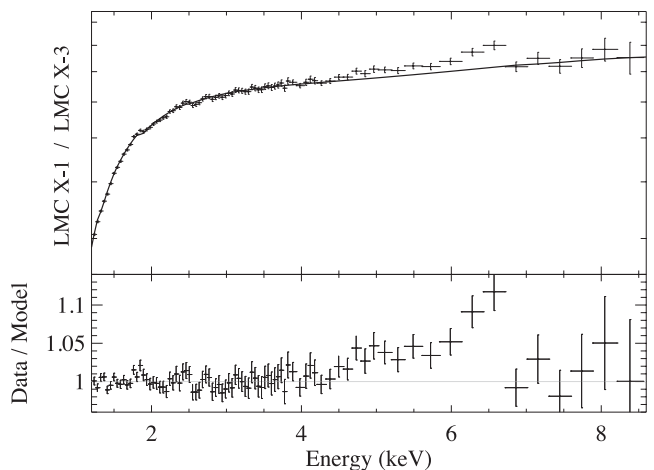
---

[10] The ISM composition in TBVARABS is taken from Hanke et al. (2009).

[11] An additional $\approx 10^5$ elements were generated during training and burn-in phases but these were not used in the final analysis (see Steiner & McClintock 2011).

[12] In all cases, a satisfactory Gelman & Rubin (1992) convergence diagnostic of $\hat{R} < 1.2$ was obtained.

[13] $N(\mu, \sigma)$ refers to a normal distribution centred upon μ with a variance of σ^2.

Figure 1. Top: ratio of the spectrum of LMC X-1 to that of LMC X-3 shown fitted to a polynomial (solid line). Bottom: the residual spectrum, which clearly reveals the presence of broadened Fe Kα emission.
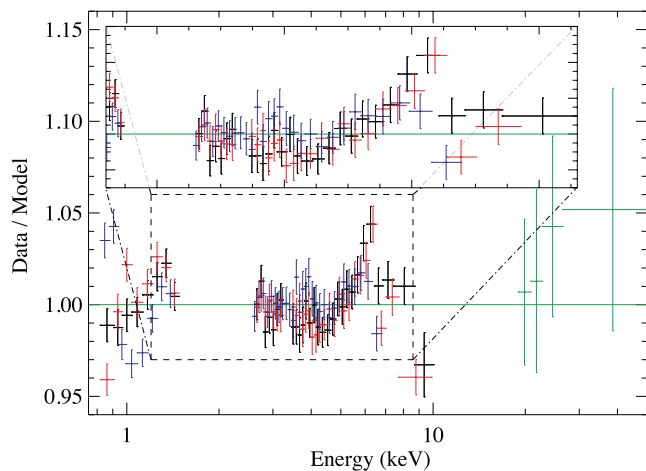
Figure 2. Residuals to the best fit of a model with Comptonized disc emission and unblurred (narrow) reflection reveal a prominent broad red wing to the Fe line in the ratio spectrum. The PIN data show a hint of curvature in the energy range of the Compton hump. These features further indicate the presence of relativistic reflection from the inner disc. Here, the data have been rebinned for plotting purposes only. To allow for a straightforward comparison, the inset highlights the same energy range as Fig. 1.

alone, it nevertheless serves to confirm the presence of LMC X-1's broad Fe line and suggests that the BH is rapidly spinning.

As a first fit to the spectral data, without yet treating effect of relativistic reflection, we apply a model of Comptonized disc emission combined with a reflection component which is unblurred and narrow [TBVARABS×(SIMPL-R⊗KERRBB2+REFLIONX)]. The data-to-model ratio for the best fit (χ^2/ν 1.2) is shown in Fig. 2, in which the residual features from 4 to 6 keV highlight an excess attributed to an unmodelled broad red wing of the Fe line. Likewise, the deficit above 8 keV and the excess and slight curvature above 20 keV indicate, respectively, the smeared Fe edge and Compton hump (although the Compton hump signal is statistically marginal). These

residual features are indicators of an untreated component of relativistically broadened reflection.

Having established the existence of gravitationally broadened spectral reflection features, we will now apply the suite of disc/reflection spectral models described above and thereby constrain LMC X-1's spin.

4.1 Spectral analysis

We begin by making the standard assumption of alignment between the BH and the binary orbital plane ($i \approx 36°$; Orosz et al. 2009), and we proceed to apply Models 1, 1p and 2 to the *Suzaku* data alone. We then follow by applying these same models to the combined *Suzaku* and *RXTE* data set. The dominance of the thermal component in the spectrum of LMC X-1, and the modest luminosity of the source (Section 1), assures that the spectrum is well described by standard thin-disc theory. Therefore, in modelling the inner reflection component, we begin by assuming that illumination of the disc follows a thin-disc profile with the standard value of the emissivity index, $q = 3$ (Fabian et al. 1989).

Fig. 3 shows our best fits to the *Suzaku* spectra for all three models. The fitting results are summarized in Table 1 [$q = 3$ results are denoted by subtypes (i) and (iii)]. MCMC is designed to directly provide posterior probability densities for the free parameters of our models. However, for large numbers of free parameters MCMC alone does not provide an optimized estimate of the minimum value of χ^2/ν. Therefore, after running the MCMC chains, in order to provide an estimate of the usual goodness of fit, we have optimized the model χ^2/ν about the central values in the chain; these optimized fits yield the χ^2/ν values given in Table 1. Although the MCMC chains do not directly deliver optimized goodness-of-fit estimates, we emphasize that the chains themselves provide the most direct estimates of the probability distributions for our model parameters, which is of chief interest.

We explore the effect of allowing q to vary and to take on the form of a broken power law [model subtypes (ii) and (iv) in Table 1].
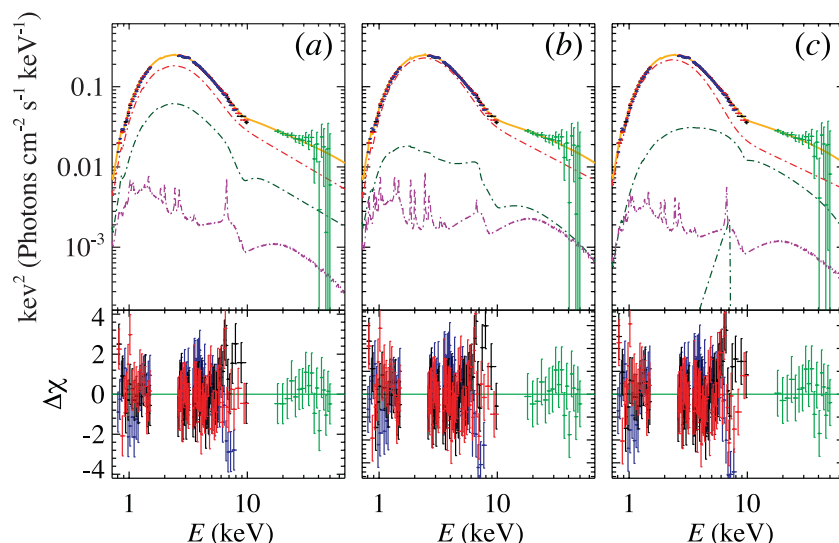

Figure 3. The unfolded spectral fit and fit residuals for LMC X-1 using all three spectral models with $q = 3$. We show the fit for Model 1 (REFBHB-M), our adopted model, in panel *a*; Model 1p (REFLIONX) in panel *b*; and Model 2 (IREFLECT) in panel *c*. The reflection signal comprises two parts: the primary comes from the inner portion of the BH's accretion disc (green lines), and the secondary from the distant gas in the system (purple lines). Comptonized disc emission is shown in red, and the composite model is overlaid in orange. In panel *a*, because REFBHB-M operates as reflection/reprocessing modifying a thermal signal, the relativistic reflection is drawn showing REFBHB-M+1.5f_{SC}(SIMPL-R⊗KERRBB2), arbitrarily chosen in order to depict a comparable normalization to panels *b* and *c*. The XIS spectra have been binned to a minimum signal-to-noise ratio of 70 for plotting only.
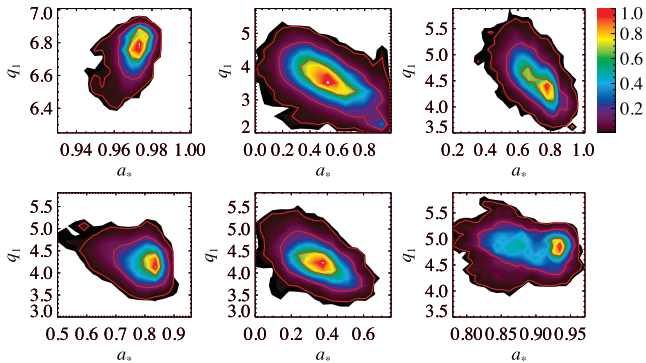
Figure 4. Selected correlation results from the MCMC analysis showing that spin and the inner emissivity index q_1 are weakly correlated. Red contours show 1σ, 2σ and 3σ confidence limits about maximum density values. Top panels correspond to *Suzaku* fitted alone [model subtype (ii)], and the bottom panels show results for *RXTE* and *Suzaku* fitted together [model subtype (iv)]. Panels on the far left use REFBHB-M (Model 1), those in the centre column use REFLIONX (Model 1p) and those on the right use IREFLECT (Model 2).

For moderate or low spins, such as those given for Model 1p, this exercise is not physically motivated, but we nevertheless use this approach to understand the effect of having initially fixed q at its canonical value of 3. Once q_1 is freed, all three models return high values, $q_1 > 3$; the outer index is fixed to $q_2 = 3$. As a net result of this exercise, the values of spin are slightly depressed. The dependence of a_* on q_1 is illustrated in Fig. 4. There is generally a weak anti-correlation between the two parameters, which is most pronounced for Models 1p (centre) and 2 (right).

Because a high value of the inner emissivity index q_1 indicates substantial light bending in the strong-gravity environment close to the BH's event horizon, one expects high q_1 to be associated with high values of spin. That we find the opposite correlation in our fits – high q_1 is associated with low spin – is simply a systematic artefact of either our model or the data, which is possibly related to the limited signal-to-noise ratio in the reflection features.

As is evident in Fig. 3, the spin is obtained by decomposing the blurred and sharp reflection components, with a substantial fraction of this signal coming from around the Fe line and edge. The sharp reflection is produced by material distant from the source, which we identify with the wind of the companion star. This subject is discussed in Section 5.3.

Overall, the three models perform comparably well. (The statistical differences in the quality of fit between Models 1, 1p and 2 are even less when one factors in the influence of the priors – an effect not captured by χ^2/ν.) However, because Model 1p uses a reflection model designed for AGN, whereas Model 1 is optimized for the densities and environments of BH binaries, we favour Model 1 because it is physically more appropriate. Model 2, which offers the most self-consistent treatment of the broad reflection continuum (while ignoring the fluorescent emission features), also returns a high spin. Model 1p is less constraining, but consistent with the others. Although we adopt the results for Model 1 which we consider to be the most physical of the three models, we use the combined results for all the models in all the columns of Table 1 to account for systematic uncertainty in our spin measurement. In particular, although their paired fits for q_1 and a_* are physically suspect (described above), we nevertheless include Model 1p(ii), Model 2(ii) and Model 1p(iv) in determining the net result. This conservative approach increases our final uncertainty.
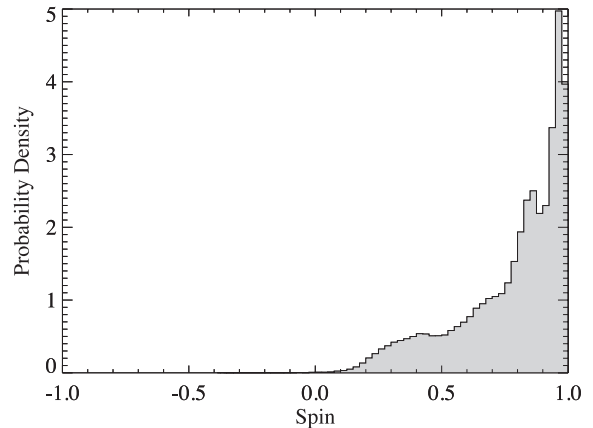

Figure 5. Our final and adopted spin probability distribution obtained by combining results from all the models in Table 1 with equal weights.

Our final result for Model 1, combining all four variants [i.e. (i)–(iv) in Table 1] is $a_* = 0.97^{+0.01}_{-0.13}$. We account for systematic effects by combining the results for all the models in all the columns of Table 1 (with equal weight assigned to each), and thereby obtain $a_* = 0.97^{+0.02}_{-0.25}$. As a firm lower bound, at 99 per cent confidence, the spin is constrained $a_* > 0.2$. This distribution, computed from the sum of all the MCMC chains, is shown in Fig. 5.

In order to assess the effect of assuming solar abundances, we explore a reduced metallicity of $Z = 0.3 Z_\odot$ for Model 1p (this metallicity setting is possible using REFLIONX but not REFBHB-M). We find an increase of $\lesssim 10$ per cent in the ISCO radius, which implies a reduction in the spin of $\Delta a_* \approx 0.02$ from our fiducial values. Metallicity is, therefore, a relatively minor source of systematic uncertainty. Similarly, we have explored the uncertainty introduced by the $1°9$ error in the orbital inclination (Orosz et al. 2009) and find that the resulting spin uncertainty is quite small ($\Delta a_* \lesssim 0.01$) compared to our net uncertainty. Lastly, one notable deficiency of Model 2 is that it omits treatment of Compton broadening of the Fe line due to scattering in the (keV-temperature) disc atmosphere. Because this temperature is far below the energy of the Fe line, Compton broadening produces an intrinsic red tail to the line (e.g. Watanabe et al. 2003; Torrejón et al. 2010). We explore this broadening by replacing the narrow Gaussian of Model 2 with a one-sided Gaussian with width $\sigma = 0.5$ keV. The width used is approximately twice as large as that due to single scattering in the disc. The broadened line returns significantly improved fits ($\Delta\chi^2 > 15$), which we interpret as a likely detection of some degree of Compton broadening. In all instances of Model 2 [i.e. (i)–(iv) in Table 1], the spin returned is in the range $a_* = 0.94$–0.98. We conclude that, because Compton broadening is an order of magnitude smaller than the maximum gravitational redshift for a rapidly spinning source, the impact on the fitted spin is moderate. Generally, accounting for this extra broadening causes the model to return a slightly lower value for spin in Model 2.

5 DISCUSSION

5.1 The connection between the Compton power law and reflection

We now explore the relationship between the most prominent feature of the reflection component, namely the Fe line, and the degree of Comptonization. To do this empirically, we make use of a
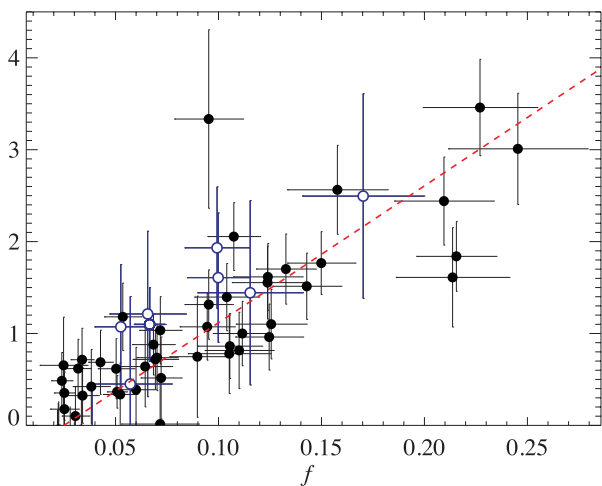
Figure 6. A strong correlation exists between the relative strength of the Compton power-law component (f_{SC}) and the Fe-line flux based on *RXTE* data. Because the simplistic model employed assumes an arbitrary linewidth, the line flux is shown to arbitrary scale. The Gou et al. (2009) spectra are displayed as closed symbols, and our observations are plotted as open symbols. A linear fit is overlaid as a dashed line.

simplified continuum model employed in Gou et al. (2009), with a small modification: TBVARABS(SIMPL⊗KERRBB2+GAUSS$_{Fe}$).[14] We apply this model to both the full Gou et al. data sample of 53 *RXTE* spectra and the *RXTE* spectra collected during our *Suzaku* observation. This model lacks the physical rigour of those we have been considering, but it has the virtue of being sensitive to the *strengths* of the Fe line and Compton component without requiring additional parametrization.[15]

As shown in Fig. 6, a clear and positive correlation is observed which is well described by a linear fit ($\chi^2/\nu = 1.17$) with a correlation that is significant at $>12\sigma$. Regardless of the geometry of the corona – whether a disc-hugging skin, a lamp-post, or a centrally concentrated cloud – the existence of this correlation confirms that the coronal Compton emission is the primary source that illuminates the disc and produces the reflection/fluorescence component in LMC X-1. This result indicates that disc self-irradiation (which could be important in producing reflection features either at high luminosities or in Compton-weak sources) is not dominant here. Our findings are in close agreement with those of Hiemstra et al. (2011), who demonstrate for the BH XTE J1652–453 the coexistence of a bright disc and strong reflection features. Hiemstra et al. point out that strong coronal flows in bright (intermediate-state) discs can produce the most prominent broad Fe lines, which may explain the strong line feature we observe in LMC X-1.

5.2 The thermal continuum

It is often problematic to use the same spectrum to estimate spin by both the continuum-fitting and Fe-line methods because the opti-

mal spectrum for continuum fitting has a weak power-law/reflection component, whereas a spectrum that is optimal for the reflection method generally has a dominant power-law component, which compromises continuum-fitting measurements. Unfortunately, for the *Suzaku* and *RXTE* spectra treated here, one cannot obtain a reliable spin measurement via continuum fitting. Despite its stable luminosity, LMC X-1 exhibits strong rms power fluctuations.[16] To obtain reliable continuum-fitting results, one generally restricts the rms power to be $\lesssim 8$ per cent (e.g. Remillard & McClintock 2006; Gou et al. 2009). However, for the spectrum in question, the rms power is in the range 27–35 per cent, and therefore a reliable continuum-fitting spin result cannot be obtained from these data.

In a study of LMC X-1's variable power-law component, Ruhlen, Smith & Swank (2011) examine the archive of *RXTE* observations of LMC X-1, and, assuming a uniform and nominal power-law index, find a weak anticorrelation between disc flux and temperature. This is exactly analogous to the anticorrelation of spin and $\dot{M}$ shown in fig. 4 of Gou et al. (2009). Ruhlen et al. interpret their flux, temperature anticorrelation as implying the presence of a variable corona that sometimes obscures the inner disc. While this interpretation is possible, it implies the occasional presence of an optically thick, ~ 50 keV coronal cloud, which has never been observed. We therefore consider this explanation unlikely. This anticorrelation may instead be related to instabilities in the disc, as suggested by the correlation between the strength of the intense power-law component and the rms variability in the power spectrum (Gou et al. 2009; and with the reflection strength, see Section 5.1). Speculatively, the variability noted by Ruhlen et al. may be consistent with the inhomogeneous-disc model of Dexter & Quataert (2012).

For any of these interpretations, the Gou et al. (2009) continuum-fitting spin measurement is robust to these effects because for measuring spin, Gou et al. selected only those data in which the Compton component is weakest ($f_{SC} < 0.075$), or equivalently, data for which the rms variability is weak. However, the continuum-fitting measurement is confounded for the *Suzaku* observation considered here.

We note that the sign and magnitude of the deviation we find for the continuum-fitting value of spin compared to the result of Gou et al. (2009) are consistent with what has been obtained for other systems; namely at excessively large values of rms, the continuum-fitting model tends to return erroneously small values of spin (e.g. fig. 1 in Steiner et al. 2009a).

Because in this instance the thermal continuum model is flawed, and additionally because Kubota et al. (2010) emphasize that a true disc spectrum may be intrinsically broader than the zero-torque KERRBB model, we examine the effect of using a modified torque at the inner-boundary. For the reasonable values we have explored, $\eta < 10$ per cent (see Li et al. 2005 for details on the torque prescription), the reflection spin measurement is insignificantly affected by this change in the continuum model. To otherwise assess the impact of our choice of thermal continuum model, we have tested replacing KERRBB2 with DISKBB (Mitsuda et al. 1984), and also with BHSPEC (Davis & Hubeny 2006) in Models 1(i), 1p(i) and 2(i). The goodness-of-fits returned with these disc models is worse by $\Delta\chi^2 \approx 20$, and the spin in each instance is consistent with $a_* > 0.9$. We conclude that our reflection spin result is robust to the choice of thermal continuum model.

---

[14] For all spectra, we use fixed values for the Gaussian line energy and width (6.5 and 0.25 keV, respectively), and use the continuum-fitting value of spin obtained by Gou et al. ($a_* = 0.92$). Further following Gou et al. (2009), we restrict the power-law index to values between $\Gamma = 2.25$ and $\Gamma = 3.25$.

[15] Because this simplistic model does not account for photoabsorption of Compton-backscattered photons, which return to the disc, the value of f_{SC} is lower here by a factor of roughly 2 compared to its value under Models 1, 1p and 2 above.

[16] We follow the convention of Remillard & McClintock (2006), who define rms variability as the average power from 0.1 to 10 Hz in the band 2–20 keV.

5.3 Distant reflection

Based on optical integral-field spectroscopy with a resolution of ∼1 pc, Cooke et al. (2008) mapped a large (≈4 pc) cone-shaped ionization nebula enshrouding LMC X-1 (Pakull & Angebault 1986). The cone has an opening angle ∼45° and a mean density on large scales of $n \lesssim 100\,\mathrm{cm}^{-3}$. Meanwhile, our spectral fits imply the presence of a strong source of reflection that is distant from LMC X-1 (i.e. separated by $r > 10^8$ cm) with a luminosity ∼10^{36}–$10^{37}\,\mathrm{erg\,s}^{-1}$.

Both the cone structure and the reflection component are readily explained at once by positing the presence of a powerful wind that is photoionized by the luminous X-ray source. We show that the wind is likely supplied by a dominant outflow from the O supergiant companion (Orosz et al. 2009) (possibly coupled with a fast wind launched from the disc). The source of illumination, meanwhile, is the self-irradiated accretion disc, which supplies the requisite flux of ionizing photons after reprocessing $\lesssim 5$ per cent of the X-rays from the inner disc into ionizing photons in the outer disc (radii $\gtrsim 100 GM/c^2$; Gierliński, Done & Page 2008; Gou et al. 2009).

Adopting a very simplified model in which reflection is approximated as efficient Thomson scattering through an idealized wind with ionization parameter ∼$10^3\,\mathrm{erg\,cm\,s}^{-1}$, we find that the wind is launched at a distance $r_0 \sim 0.2$ au from the BH and with a density of $n_0 \sim 10^{10}\,\mathrm{cm}^{-3}$. These values match the BH-to-companion star distance and the surface density in its stellar wind (Lamers & Leitherer 1993; Orosz et al. 2009); this identifies the stellar wind as the likely source of distant ionized gas. At sub-pc scales, the ionization of the wind is constant ($n \propto r^{-2}$), but because density falls off rapidly, most of the (sharp) reflection is centrally concentrated and emitted from the innermost several au.

Meanwhile, at parsec scales, the wind is shocked against the ambient interstellar medium (ISM). As a result, the ionization cone is mostly filled with a dense gas of shocked wind. This cone, in turn, is enclosed in a thin shell of even denser shocked ISM (e.g. Weaver et al. 1977). This picture is borne out by the flat temperature and density profiles[17] within the ionization cone, which are shown in Fig. 7.

Adopting this simplistic description of the wind as valid, and employing the Weaver et al. (1977) wind-bubble model, the projected mass in the wind is of the order of ∼$0.1\,\mathrm{M}_\odot$, which suggests a time-scale of ∼10^6 yr to produce the ionization cone surrounding LMC X-1.[18] The mass in the cone is then commensurate with the integrated mass loss from the companion star, and a time-scale results which is comparable to the ≈5 Myr age of the system (Orosz et al. 2009).

6 CONCLUSIONS

We have analysed a deep *Suzaku* and *RXTE* observation of LMC X-1, and have demonstrated that a broad Fe Kα line is present

Figure 7. Radial profiles for the density and gas temperature in the ionization cone are approximately flat. This supports our assertion that the optical ionization cone is a shell of shocked interstellar gas. This gas encloses a bubble inflated by the stellar wind (e.g. compare with the 'shell' region in fig. 3 of Weaver et al. 1977).

in the spectrum of the source. Using existing and new spectral reflection models, we have measured the BH's spin parameter to be $a_* = 0.97^{+0.01}_{-0.13}$ for our favoured model (Model 1), and to be $a_* = 0.97^{+0.02}_{-0.25}$ when making an allowance for systematic error by considering our full range of models. At 99 per cent confidence, we establish $a_* > 0.2$. Both of these spin estimates are in agreement with the spin determined using the X-ray continuum-fitting method (Gou et al. 2009).

Apart from the measurement of spin, we present two additional results: (1) for a large sample of *RXTE* spectra, we demonstrate a strong and positive correlation between the Compton and reflection components. (2) Far from the strong gravity environment of the BH, we identify the wind of the massive companion star as the source of a luminous and sharp reflection component. We conclude that the wind and persistent X-ray source together maintain the parsec-scale ionization cone that envelops the binary system.

---

[17] These profiles are derived from the data in Cooke et al. (2008) by using the [S II] λλ6716/6731 ratio as a density diagnostic and the [O III] λλ(4959+5007)/4363 ratio as a temperature diagnostic (Osterbrock & Ferland 2006). See Cooke et al. (2008) for more details.

[18] Derived using the ISM density in LMC X-1's local environment (an O-B association) of ∼$20\,\mathrm{cm}^{-3}$. This, in turn, is obtained by assuming the standard jump condition at the outer shock boundary given that the density in Fig. 7 corresponds to the high-density outer shell.
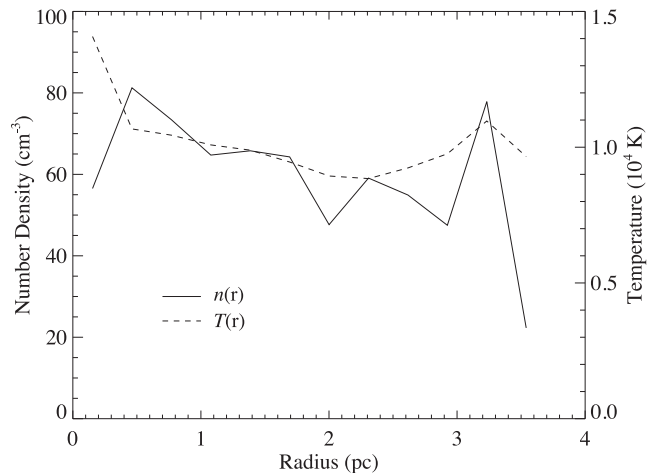
REFERENCES

Arnaud K. A., 1996, in Jacoby G. H., Barnes J., eds, ASP Conf. Ser. Vol. 101. Astronomical Data Analysis Software and Systems V. Astron. Soc. Pac., San Francisco, p. 17

Brenneman L. W., Reynolds C. S., 2006, ApJ, 652, 1028

Cooke R., Bland-Hawthorn J., Sharp R., Kuncic Z., 2008, ApJ, 687, L29

Dauser T., Wilms J., Reynolds C. S., Brenneman L. W., 2010, MNRAS, 409, 1534

Davis S. W., Hubeny I., 2006, ApJS, 164, 530

Dexter J., Quataert E., 2012, MNRAS, L512

Done C., Gierliński M., Kubota A., 2007, A&AR, 15, 1

Fabian A. C., Rees M. J., Stella L., White N. E., 1989, MNRAS, 238, 729

Fabian A. C. et al., 2012, MNRAS, 424, 217

Foreman-Mackey D., Hogg D. W., Lang D., Goodman J., 2012, preprint (arXiv:1202.3665)

Fukazawa Y. et al., 2009, PASJ, 61, 17

Gelman A., Rubin D., 1992, Stat. Sci., 7, 457

Gierliński M., Done C., Page K., 2008, MNRAS, 388, 753

Gilfanov M., 2010, in Belloni T., ed., Lecture Notes in Physics, Vol. 794, X-Ray Emissions from Black-Hole Binaries. Springer-Verlag, Berlin, p. 17

Gou L. J. et al., 2009, ApJ, 701, 1076

Haardt F. et al., 2001, ApJS, 133, 187

Hanke M., Wilms J., Nowak M. A., Pottschmidt K., Schulz N. S., Lee J. C., 2009, ApJ, 690, 330

Hiemstra B., Méndez M., Done C., Díaz Trigo M., Altamirano D., Casella P., 2011, MNRAS, 411, 137

Ishida M. et al., 2011, PASJ, 63, 657

Kubota A., Done C., Davis S. W., Dotani T., Mizuno T., Ueda Y., 2010, ApJ, 714, 860

Kulkarni A. K. et al., 2011, MNRAS, 414, 1183

Lamers H. J. G. L. M., Leitherer C., 1993, ApJ, 412, 771

Li L.-X., Zimmerman E. R., Narayan R., McClintock J. E., 2005, ApJS, 157, 335

McClintock J. E., Shafee R., Narayan R., Remillard R. A., Davis S. W., Li L.-X., 2006, ApJ, 652, 518

Magdziarz P., Zdziarski A. A., 1995, MNRAS, 273, 837

Miller J. M., 2007, ARA&A, 45, 441

Miller J. M., Reynolds C. S., Fabian A. C., Miniutti G., Gallo L. C., 2009, ApJ, 697, 900

Miller J. M. et al., 2010, ApJ, 724, 1441

Mitsuda K. et al., 1984, PASJ, 36, 741

Noble S. C., Krolik J. H., Hawley J. F., 2009, ApJ, 692, 411

Noble S. C., Krolik J. H., Schnittman J. D., Hawley J. F., 2011, ApJ, 743, 115

Nowak M. A., Wilms J., Heindl W. A., Pottschmidt K., Dove J. B., Begelman M. C., 2001, MNRAS, 320, 316

Nowak M. A. et al., 2011, ApJ, 728, 13

Orosz J. A. et al., 2009, ApJ, 697, 573

Osterbrock D. E., Ferland G. J., 2006, Astrophysics of Gaseous Nebulae and Active Galactic Nuclei. University Science Books, Sausalito, CA

Pakull M. W., Angebault L. P., 1986, Nat, 322, 511

Penna R. F., McKinney J. C., Narayan R., Tchekhovskoy A., Shafee R., McClintock J. E., 2010, MNRAS, 408, 752

Reis R. C., Fabian A. C., Ross R. R., Miniutti G., Miller J. M., Reynolds C., 2008, MNRAS, 387, 1489

Remillard R. A., McClintock J. E., 2006, ARA&A, 44, 49

Reynolds C. S., Fabian A. C., 2008, ApJ, 675, 1048

Ross R. R., Fabian A. C., 2005, MNRAS, 358, 211

Ross R. R., Fabian A. C., 2007, MNRAS, 381, 1697

Ruhlen L., Smith D. M., Swank J. H., 2011, ApJ, 742, 75

Schnittman J. D., Krolik J. H., Noble S. C., 2012, preprint (arXiv:1207.2693)

Shafee R., McKinney J. C., Narayan R., Tchekhovskoy A., Gammie C. F., McClintock J. E., 2008, ApJ, 687, L25

Steiner J. F., McClintock J. E., 2011, ApJ

Steiner J. F., McClintock J. E., Remillard R. A., Narayan R., Gou L. J., 2009a, ApJ, 701, L83

Steiner J. F., Narayan R., McClintock J. E., Ebisawa K., 2009b, PASP, 121, 1279

Steiner J. F., McClintock J. E., Remillard R. A., Gou L., Yamada S., Narayan R., 2010, ApJ, 718, L117

Steiner J. F. et al., 2011, MNRAS, 416, 941

Toor A., Seward F. D., 1974, AJ, 79, 995

Torrejón J. M., Schulz N. S., Nowak M. A., Kallman T. R., 2010, ApJ, 715, 947

Tsujimoto M. et al., 2011, A&A, 525, A25

Watanabe S. et al., 2003, ApJ, 597, L37

Weaver R., McCray R., Castor J., Shapiro P., Moore R., 1977, ApJ, 218, 377

Wilkins D. R., Fabian A. C., 2011, MNRAS, 414, 1269

Wilms J., Allen A., McCray R., 2000, ApJ, 542, 914

Wilms J., Nowak M. A., Pottschmidt K., Heindl W. A., Dove J. B., Begelman M. C., 2001, MNRAS, 320, 327

Zhang S. N., Cui W., Chen W., 1997, ApJ, 482, L155

Zhu Y., Davis S. W., Narayan R., Kulkarni A. K., Penna R. F., McClintock J. E., 2012, MNRAS, 424, 2504

This paper has been typeset from a TEX/LATEX file prepared by the author.